

Inversion of the Sound Speed With Radiated Noise of an Autonomous Underwater Vehicle in Shallow Water Waveguides

Ming Zhang, Wen Xu, *Senior Member, IEEE*, and Yuanxin Xu

Abstract—In December 2013, an experiment using an autonomous underwater vehicle (AUV) as a moving source for water column sound speed profile (SSP) inversion was conducted in Mogan Lake, China. With *in-situ* conductivity, temperature, and depth (CTD) measurements, the empirical orthogonal functions were first constructed to represent the SSP. Radiated noises of the AUV were received on a vertical line array and processed via acoustic field matching to obtain estimates of the range-independent SSP, along with the position and velocity of the AUV and the water column depth. The frequency of the radiation noise of the AUV was approximately 14 kHz. At such high frequency, even though the source motion was slow, a significant Doppler shift/broadening was observed. To incorporate the Doppler effects to better match the measured data, a forward acoustic model is derived based on the waveguide Doppler and normal mode theory. An analytical solution of the forward model is obtained for arbitrary signal integration intervals with a monochromatic source, moving radially relative to the receiver. Through simulations and experimental data processing, the feasibility of using an AUV source for water column SSP inversion has been demonstrated; it is also shown that the waveguide Doppler model is more effective compared with the model that does not consider the waveguide Doppler effect.

Index Terms—Autonomous underwater vehicle (AUV), matched-field inversion, moving source, radiated noise, sound speed profile (SSP), waveguide Doppler.

I. INTRODUCTION

THE sound speed profile (SSP) in the water column is one of the most important parameters in determining acoustic waveguide propagation. Meanwhile, it provides an important source of information to extract ocean properties such as temperature. For example, the so-called ocean acoustic tomography (OAT) [1] proposed by Munk and Wunsch can infer the state of the interior of the survey domain from measurements along the periphery using travel-time inversion [1], [2] or matched-field inversion [3], [4] in a large scale. However, the ocean, especially the coastal environment, has variability over a wide range

Manuscript received September 16, 2014; revised March 10, 2015; accepted March 24, 2015. Date of publication April 27, 2015; date of current version January 11, 2016. This work was supported by the National High Technology Research and Development Program of China (Grant 2012AA090901 and 2013AA09A414). Corresponding Author: Yuanxin Xu.

Associate Editor: N. R. Chapman.

The authors are with the Department of Information Science and Electronic Engineering, Zhejiang University, Hangzhou 310027, China (e-mail: 05xxgczm@zju.edu.cn; wxu@zju.edu.cn; xuyx@zju.edu.cn).

Digital Object Identifier 10.1109/JOE.2015.2418172

of spatial and temporal scales. To obtain measurements that cover large area as well as having fine resolution, Schmidt *et al.* proposed new oceanographic measurement concepts, such as Adaptive Rapid Environment Assessment [5] and Acoustically Focused Oceanographic Sampling [6], [7]. The basic idea is using OAT to provide a low-resolution, but synoptic estimate of the environment, while guiding the moving nodes, such as autonomous underwater vehicles (AUVs), into areas of high uncertainty to perform small-scale high-resolution measurements of the environment.

For the purpose of OAT, an AUV can act as a moving receiver, a moving source, or both. For example, Holmes *et al.* [8] used a ship-deployed continuous wave source and an AUV with a towed array to obtain range-independent sediment properties; Leijen *et al.* [9] used radiated noise of an AUV received on a vertical line array (VLA) to invert the geoacoustic parameters; Chotiros *et al.* [10] used radiation noise of an AUV, in conjunction with its towed array, to measure the bottom reflection loss and obtain an estimate of the seabed type. However, research work using the AUV as a moving source to invert the water column SSP are rarely seen in the existing literatures.

It is common to measure the sound speed directly with conductivity, temperature, and depth (CTD) sensors mounted on the AUV; however, the AUV needs to survey the entire water column to sample the depth-dependent SSP. This can be quite time-consuming, especially when the water depth is large and/or the environment is highly time-varying. The acoustic inversion approach with the AUV as a moving source (assuming its self-radiation is strong enough or it can carry a proper sound source) provides an efficient way to estimate the range-averaged SSP. The AUV only needs to run outside the survey domain at a constant depth. Indeed, using the range-averaged SSP is more appropriate for model-based sonar processing, e.g., matched-field geoacoustic inversion [11], than using a single SSP measured at a specific site. With the AUV traveling along certain paths, it may even get a three-dimensional field picture by combining range-averaged SSPs measured at individual points. Moreover, for conventional OAT with fixed source depths, it may not able to produce a good ray structure observed at the receiver for inversion; with AUV adaptively changing depth, one may obtain optimum source excitation for inversion. This adaptively can be fully exploited by combining the acoustic inversion approach with AUV-carried CTD measurements. Meanwhile, the inversion approach allows tracking of the AUV since it can invert the position (depth and range) of the AUV simultaneously. Devel-

opment of the above concepts does rely on maturing of the AUV technology, which is becoming reality now in both the research community and industry.

To evaluate the feasibility of using the AUV as a moving source for water column SSP inversion, an experiment was conducted in Mogan Lake, China, in December 2013. Instead of using controlled sonar transmissions, the radiation noise of the AUV was used as a sound source; a VLA with 16 elements was deployed nearby spanning most of the water column. Matched-field inversion is used to invert the SSP, the position and velocity of the AUV, as well as the water depth in a range-independent environment. During the experiment, the AUV carried out two types of constant depth missions, one traversing a set of waypoints on a circular path, the other traversing a set of waypoints along the radial direction, both of which position the VLA as the center point. This paper mainly focuses on the data of the radial direction mission. The frequency of the AUV radiation was approximately 14 kHz. At such high frequency the acoustic field is very sensitive to the source range and depth. Hence compared with the low frequency, the quasistationary time of the observed field becomes shorter. In addition, even though the source motion is slow there can be a significant Doppler shift/broadening because of the high source frequency. As such, the waveguide Doppler effect [12], [13] of the moving source needs to be considered.

Due to the waveguide effect, different modes (grazing angles) have different Doppler shifts, i.e., each modal component propagates at a distinct frequency. Schmidt *et al.* [12], [14] derived a spectral representation of the Doppler-shifted field in a range-independent waveguide environment. The derived formulation can be incorporated into the existing normal mode model, allowing for numerical evaluation of each modal component. Tan *et al.* [15] adopted this waveguide Doppler and normal mode theory to synthesize the forward model for broadband frequency coherent matched-field inversion with a moving source. However, the frequency resolution of the received field is dependent on the signal integration interval or the range aperture traversed by the source. As pointed out by Walker *et al.* [16], the range aperture has to be large enough (several modal interference length) to resolve modal Doppler shifted frequencies. For the frequency of 14 kHz and water depth of 20 m, a minimum of 2.8 km of range aperture is required to extract modes 1 and 2 from the received field. Even if the AUV can move stably (constant velocity and constant depth) over such a large distance, the range-independent condition is hard to meet.

In the case that the modal Doppler shifted frequency is unresolvable, the frequency response of the received field is a weighted sum of the modal components, thus the waveguide Doppler model derived in [12] can not be used directly as the forward model. In this paper, for a monochromatic source moving radially relative to the receiver, an analytical solution of the forward model is derived based on the waveguide Doppler model but for arbitrary signal integration intervals. Because the waveguide Doppler model is computationally intensive, especially when the frequency is high, to reduce the computational complexity, a simplified model is proposed. Given that the weight of each modal component is determined by the range aperture or signal integration interval, the performances

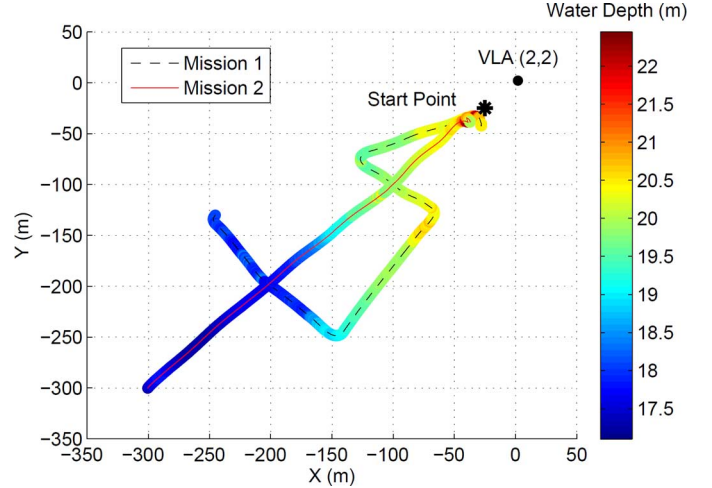


Fig. 1. Trajectories of AUV in two distinct missions and the water depth along the trajectories.

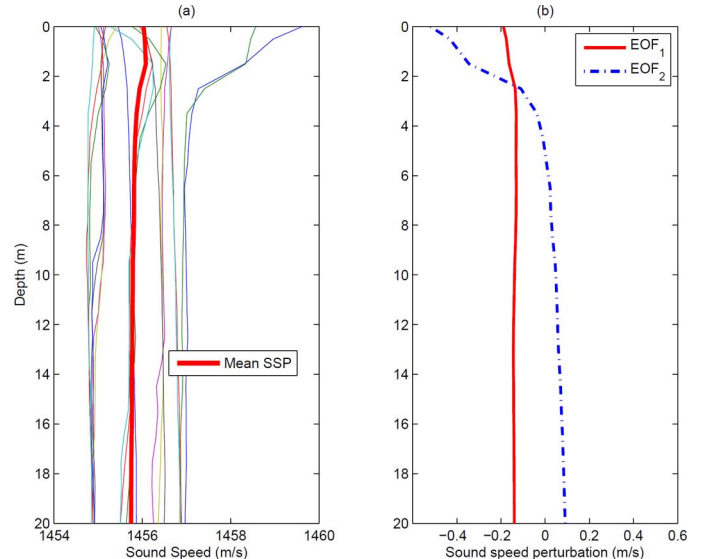


Fig. 2. (a) SSPs of 18 CTD casts during the experiment and their average profile. (b) The first two EOFs.

of inversions are compared at different integration intervals with synthetic and experimental data. The results using the model that does not consider waveguide Doppler effects are also presented for comparison.

The remainder of the paper is organized as follows. The experimental setup is introduced in Section II. The forward acoustic model based on the waveguide Doppler model is then derived in Section III, followed by definition of the objective function of the inversion problem. Simulations based on the experimental configuration are presented in Section IV. Inversion results with experimental data are presented in Section V. Finally, Section VI concludes the paper.

II. EXPERIMENT AND DATA DESCRIPTION

Section II-A describes the experimental setup, including the geometry of the experiment area, the trajectory of the AUV, and

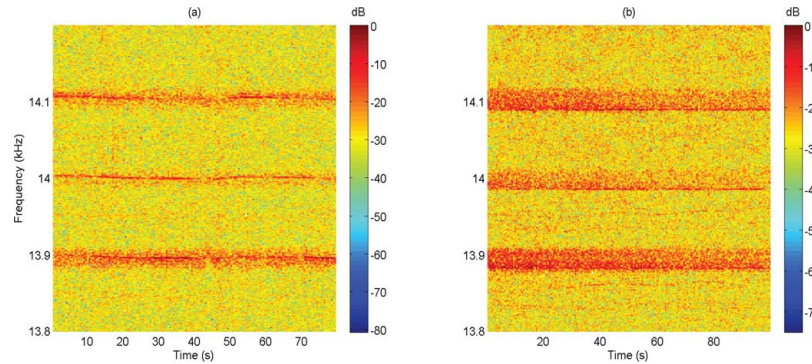


Fig. 3. Spectrogram from 13.8 to 14.2 kHz. (a) The received data of Mission 1 (Fig. 1) from point $(-150 \text{ m}, -250 \text{ m})$ to $(-240 \text{ m}, -150 \text{ m})$. (b) The received data of Mission 2 (Fig. 1) from point $(-100 \text{ m}, -100 \text{ m})$ to $(-200 \text{ m}, -200 \text{ m})$.

the SSPs. Features of the noise radiated from the AUV are presented in Section II-B.

A. Geometry, AUV Trajectory, and SSPs

The experiment was conducted in Mogan Lake on December 11–13, 2013. The AUV uses a GPS, with an accuracy of about 10 m, for surface navigation. GPS measurement stops when the vehicle dives, then the vehicle derives position estimates from an inertial navigation system, whose relative error is less than 1% of the travelling distance. The depth and altitude values of the AUV are from a pressure sensor, and a Doppler Velocity Log, respectively. The depth of water column is the sum of those two values. A detailed and complete description of the AUV can be found in [17]. The geometry of the experimental area and the trajectories of the AUV are shown in Fig. 1. The experimental area is a rectangular box with water depth of about 20 m. The bottom between the VLA (2 m, 2 m) and point $(-150 \text{ m}, -150 \text{ m})$ is relatively flat. The AUV performed two distinct constant depth (5 m) missions at a speed of 1.4 m/s. At the beginning of Mission 1, the AUV started its run close to the VLA, went off to about 144 m from the VLA, and then traveled along a circular path around the VLA. The AUV then repeated this pattern once at VLA range of 286 m. In Mission 2, the AUV traveled away from the VLA, and tracked the waypoints on the radial direction. The coordinate of the furthest point AUV reached was $(-300 \text{ m}, -300 \text{ m})$.

SSPs were measured near the location of VLA by CTD every 1–2 h in the daytime during the experiment. Fig. 2(a) shows an ensemble of 18 CTD casts and their average values. The first two empirical orthogonal functions (EOFs) [18] are shown in Fig. 2(b), which, in terms of energy, describe 98.86% of the sound speed variation. The first EOF mainly represents the variability of the sound speed over the entire water column. Two SSPs measured at noon have a slightly negative profile close to the surface. Sound speed uncertainties associated with the surface temperature changes are mainly modeled by the second EOF. Because the air temperature stays relatively low, the SSPs show small variation with time and depth. The first two EOF coefficients for those CTD measurements vary from -7.0 to 9.8 and -1.61 to 2.46 , respectively. To cope with the real environment which might have larger SSP variations over those represented by the CTD measurements, we increase the search inter-

vals of the first two EOF coefficients to $[-20\ 20]$ and $[-10\ 10]$, respectively.

The VLA consists of 16 elements with an equal spacing of 1 m. Two self-recording temperature and depth sensors were fixed at the 1st (the topmost element) and 16th elements to monitor the depth and tilt of the VLA. The depth of the 1st element was measured to be 1.5 m. As the lake was quite stationary during the experiment, the array tilt was less than 1 degree. The signals received by the VLA were first preamplified and then digitized with a 50-kHz sampling rate.

B. AUV-Radiated Noise

Holmes *et al.* [19] studied the characteristics of the radiation noise of small-to-medium AUVs, and found that most of AUVs radiate narrow-band noise ranging from 1 to 16 kHz. The AUV we used has an overall length of 2 m with a body diameter of 20 cm [17]. Spectrograms of the received data were produced using a 65 536-point fast Fourier transform with a Hamming window of length 65 536 and 50% overlap of time snapshots between adjacent processing blocks. Fig. 3 shows the spectrogram of the signal received by the 5th element of the VLA. Fig. 3(a) shows the spectrogram of Mission 1 [see Fig. 1] from point $(-150 \text{ m}, -250 \text{ m})$ to $(-240 \text{ m}, -150 \text{ m})$ where the radial velocity was approximately zero. Fig. 3(b) shows the spectrogram of Mission 2 [see Fig. 1] from point $(-100 \text{ m}, -100 \text{ m})$ to $(-200 \text{ m}, -200 \text{ m})$ where the radial velocity was approximately 1.4 m/s. There are clearly three fixed spectral lines between 13.8 and 14.2 kHz in Fig. 3(a), while the spectral lines are broadened in Fig. 3(b) due to the waveguide Doppler effect. Fig. 4 shows the normalized power spectral density of the data in Fig. 3(a) from 12 to 21 s. The dashed line indicates the background noise of the 6-s data prior to the mission. The frequencies of three tones are 13 896, 14 000, and 14 103 Hz, respectively. This paper mainly uses the 13 896-Hz tone for analysis due to the relative high signal-to-noise ratio (SNR), for which the source level was estimated to be 112 dB re $1 \mu\text{Pa}$ at 1 m.

III. THEORY

The inversion is based on matched-field processing, and the process involves a forward acoustic model to predict the received acoustic field and an objective function to be optimized. EOFs are employed to reduce the degrees of freedom of SSP.

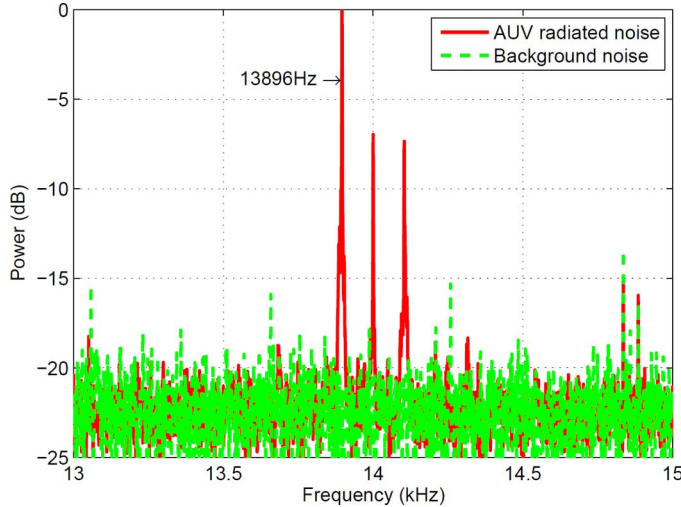


Fig. 4. Normalized mean power spectral density from 13 to 15 kHz of Mission 1 [data in Fig. 3(a) from 12 to 21 s] and the background noise (6-s data prior to the mission).

A. Forward Acoustic Model

The forward acoustic model is derived based on the waveguide Doppler and normal mode theory [12], [14]. Fig. 5 illustrates a horizontally stratified ocean environment in Cartesian coordinates. The source and the VLA have a relative motion in the horizontal direction. Assume that the source has a velocity vector of \mathbf{v}_s and the VLA is moving with a velocity vector of \mathbf{v}_r . The angles between the velocity vectors and the radial vector connecting source and VLA are denoted as θ_s and θ_r , respectively. In the waveguide, due to source and/or receiver motion, each horizontal wavenumber component of the acoustic field will undergo a different Doppler shift. For a moving harmonic point source with a source spectrum of $S(\Omega_s)$, the normal mode representation of the Doppler shifted acoustic field is [12], [14], [15]

$$\psi(\mathbf{r}, z, \omega_r) \simeq \frac{i}{4\rho(z_s)} \sum_n S(\Omega_s^{(k_n)}) \times \Psi_n(z; \omega_p) \Psi_n(z_s; \omega_p) H_0^{(1)}(k_n r_0) \quad (1)$$

where:

- $\psi(\mathbf{r}, z, \omega_r)$ is the receiving pressure value of the Doppler shifted frequency ω_r (assuming that the integration interval is long enough to separate the adjacent Doppler shifted frequencies), $\mathbf{r} = \mathbf{r}_0 + \mathbf{v}_r t$ represents the receiver position vector, and $r_0 = |\mathbf{r}_0|$ is the source-receiver range at $t = 0$.
- $\rho(z_s)$ is the water density at source depth z_s .
- $S(\Omega_s^{(k_n)})$ is the source spectrum of the source frequency $\Omega_s^{(k_n)}$, with

$$\Omega_s^{(k_n)} = \omega_r - k_n(v_s - v_r) \quad (2)$$

where $v_s = |\mathbf{v}_s| \cos \theta_s$, $v_r = |\mathbf{v}_r| \cos \theta_r$, k_n represents the propagation modal wavenumber, with

$$k_n \simeq \frac{k_{rn}}{(1 - \frac{v_r}{u_{rn}})} \quad (3)$$

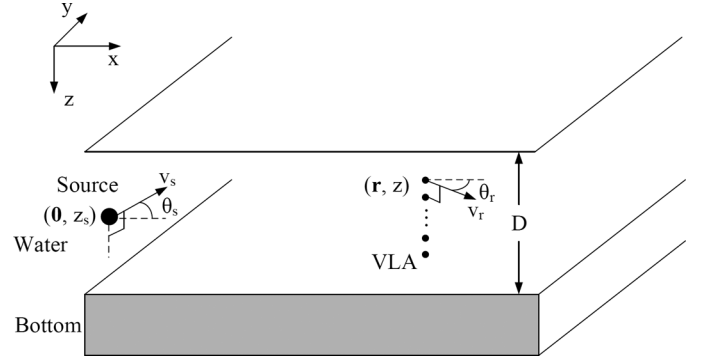


Fig. 5. Horizontally stratified waveguide environment with horizontally moving source and receiver.

and k_{rn} and $u_{rn} = d\omega_r/dk_{rn}$ are the n th wavenumber and modal group velocity, respectively, both evaluated at ω_r . Equation (2) means that different source frequencies $\Omega_s^{(k_n)}$ can generate the same Doppler shifted frequency ω_r with corresponding k_n .

- $\sum_n(\cdot)$ indicates that $\psi(\mathbf{r}, z, \omega_r)$ is a summation of source spectrum weighted modal components, where the source frequencies and wavenumbers are determined by (2).
- $\Psi_n(z; \omega_p)$ is the modal depth function evaluated at the propagation frequency ω_p , with

$$\omega_p = \omega_r + k_n v_r. \quad (4)$$

$$\bullet \quad H_0^{(1)}(k_n r_0) \simeq \sqrt{2/\pi k_n r_0} e^{i(k_n r_0 - \pi/4)}.$$

In (1), it has assumed that:

- 1) the velocities of source and VLA are much less than the sound speed in water column, i.e., $v_s/c \ll 1$, and $v_r/c \ll 1$;
- 2) the source and VLA have a uniform motion in the horizontal direction, and the velocities in depth are both zero. In addition, the radial velocities are constant.

In this paper, we consider a monochromatic source with a frequency of ω_s , and a stationary VLA, i.e., $v_r = 0$. Substituting $v_r = 0$ into (3) and (4), we have $k_{rn} = k_n$ and $\omega_r = \omega_p$. Then (2) can be simplified as

$$\omega_s = \omega_r - k_{rn} v_s. \quad (5)$$

Since a monochromatic point source is considered here, from (5) it is seen that there is a one-to-one relationship between k_{rn} and ω_r , i.e., each mode propagates at a distinct frequency.

Assume that there are L Doppler shifted frequencies ω_r^l , $l = 1, 2, \dots, L$. For the l th Doppler shifted frequency ω_r^l , the associated horizontal wavenumber that satisfies (5) is $k_{rn_l}^l$. The superscript l of $k_{rn_l}^l$ indicates that it is evaluated at the l th Doppler shifted frequency, and the subscript n_l indicates that it is the n_l th horizontal wavenumber that satisfies (5). We denote the corresponding modal depth function as $\Psi_{n_l}(z; \omega_r^l)$. Equation (1) then becomes

$$\psi(\mathbf{r}_0, z, \omega_r^l) \simeq \frac{i}{4\rho(z_s)} S(\omega_s) \times \Psi_{n_l}(z; \omega_r^l) \Psi_{n_l}(z_s; \omega_r^l) H_0^{(1)}(k_{rn_l}^l r_0) \quad (6)$$

where $S(\omega_s)$ is the source spectrum at frequency ω_s , which is assumed to be a constant. Equation (6) means that the pressure field of a single Doppler shifted frequency is generated by one modal component. To obtain the result given in (6), we have to compute ω_r^l and $k_{rn_l}^l$ using (5). However, it is difficult to find an analytic solution [16]; instead we seek an approximate solution for ω_r^l and $k_{rn_l}^l$, which is described in the Appendix.

The received pressure field in (6) is based on the condition that the integration interval is long enough to separate the adjacent Doppler shifted frequencies. From the discussions in Section I, we would have to face the situation with short range aperture and thus a pressure field representation for an arbitrary integration interval is highly desired. We denote $p(\mathbf{r}_0, z, t)$ as the pressure field in time domain, which can be expressed as

$$p(\mathbf{r}_0, z, t) = \sum_{l=1}^L \psi(\mathbf{r}_0, z, \omega_r^l) e^{i\omega_r^l t}. \quad (7)$$

The Fourier transform of $p(\mathbf{r}_0, z, t)$ is $\sum_{l=1}^L 2\pi \psi(\mathbf{r}_0, z, \omega_r^l) \delta(\omega - \omega_r^l)$. Applying the Fourier transform to (7) from time 0 to T (recall that source-receiver range is r_0 when $t = 0$), the received pressure field at frequency ω is (to distinguish it from source frequency and Doppler shifted frequency, we call ω the receiver frequency following [12])

$$\begin{aligned} \tilde{p}(\mathbf{r}_0, z, \omega) &= \int_{-\infty}^{\infty} p(\mathbf{r}_0, z, t) w(t) e^{-i\omega t} dt \\ w(t) &= \begin{cases} 1, & 0 < t < T \\ 0, & \text{otherwise.} \end{cases} \end{aligned} \quad (8)$$

Since $w(t)$ is a rectangular window function, its Fourier transform is a sinc function. Thus, according to the property of Fourier transform, (8) can be expressed as

$$\tilde{p}(\mathbf{r}_0, z, \omega) = \sum_{l=1}^L \frac{2e^{-i(\omega - \omega_r^l)T/2} \sin[(\omega - \omega_r^l)\frac{T}{2}]}{\omega - \omega_r^l} \psi(\mathbf{r}_0, z, \omega_r^l) \quad (10)$$

where T represents the integration interval. The model of (10) is referred to as M1. It is a weighted sum of the modal components, and the weight of each modal component is determined by the range aperture or signal integration interval. From (10) it is seen that the adjacent Doppler shifted frequencies can be resolved when

$$|\omega_r^l - \omega_r^{l+1}| \frac{T}{2} \gg \pi. \quad (11)$$

Substituting (5) into (11) yields

$$\left| (k_{rn_l}^l - k_{rn_{l+1}}^{l+1}) v_s \right| \gg \frac{2\pi}{T} \quad (12)$$

which means that the source should move stably at a range of

$$R = v_s T \gg \frac{2\pi}{|(k_{rn_l}^l - k_{rn_{l+1}}^{l+1})|}. \quad (13)$$

When (13) is satisfied, the received field can be approximated by

$$\tilde{p}(\mathbf{r}_0, z, \omega) \simeq T \sum_{l=1}^L \psi(\mathbf{r}_0, z, \omega_r^l) \delta(\omega - \omega_r^l). \quad (14)$$

From (10) it is seen that one would need L normal mode model runs to compute all the modal components to obtain the pressure at receiver frequency ω . For high source frequency, L is large, and some approximate solutions should be developed to improve the computational efficiency. In [13] and [16], it is assumed that $\Psi_{n_l}(z; \omega_r^l) \simeq \Psi_l(z; \omega_s)$, $k_{rn_l}^l \simeq k_{rl}(\omega_s)$, and modal cutoffs/additions are neglected when the velocity of source is small, i.e., there are L modal components evaluated at ω_s . Since ω is closer to ω_r^l compared with ω_s , it may make more sense to take the approximation that $\Psi_{n_l}(z; \omega_r^l) \simeq \Psi_l(z; \omega)$ and $k_{rn_l}^l \simeq k_{rl}(\omega) \triangleq k_{rl}$. Thus we have

$$\psi(\mathbf{r}_0, z, \omega_r^l) \simeq \psi(\mathbf{r}_0, z, \omega, k_{rl}) \quad (15)$$

$$\omega_r^l = \omega_s + k_{rl} v_s \quad (16)$$

where $\psi(\mathbf{r}_0, z, \omega, k_{rl})$ is the pressure value evaluated at receiver frequency ω and wavenumber k_{rl} with (6). Then (10) can be simplified as

$$\tilde{p}(\mathbf{r}_0, z, \omega) \simeq \sum_{l=1}^L \times \frac{2e^{-i(\omega - \omega_r^l)T/2} \sin[(\omega - \omega_r^l)\frac{T}{2}]}{\omega - \omega_r^l} \psi(\mathbf{r}_0, z, \omega, k_{rl}). \quad (17)$$

The model of (17) is referred to as M2. The number of the Doppler shifted frequencies of M2 equals to the number of modes or wavenumbers evaluated at receiver frequency ω .

The second simplified method considers that each modal component has a unit weight, i.e.

$$\tilde{p}(\mathbf{r}_0, z, \omega) \simeq \sum_{l=1}^L \psi(\mathbf{r}_0, z, \omega, k_{rl}). \quad (18)$$

The model of (18) will be referred to as M3. M3 is independent of source velocity, and thus it does not consider the waveguide Doppler effect. Indeed M3 is the general model for low frequency moving source inversion. For low source frequency, the Doppler broadening $|\omega_r^1 - \omega_r^L|$ is smaller compared to that of high source frequency, which makes the weight of each modal component approaching the same value when T is small. M2 and M3 both need only one normal mode model run to obtain the pressure value at receiver frequency ω .

B. Empirical Orthogonal Function Representation of SSP

To reduce the degrees of freedom of SSP, EOFs are employed to describe the SSP perturbations. Assuming that there are N_J SSP measurements, the mean SSP can be represented as

$$\mathbf{c}_0 = \frac{1}{N_J} \sum_{j=1}^{N_J} \mathbf{c}_j \quad (19)$$

where $\mathbf{c}_j = [c_j(Z_1) \ c_j(Z_2) \ \dots \ c_j(Z_{N_Z})]^T$ is the vector of the j th SSP measurement at N_Z discrete depth points. The sample covariance matrix is given by

$$\boldsymbol{\Upsilon} = \frac{1}{N_J} \sum_{j=1}^{N_J} (\mathbf{c}_j - \mathbf{c}_0)(\mathbf{c}_j - \mathbf{c}_0)^T. \quad (20)$$

Using the orthogonal decomposition, we have

$$\Upsilon = \sum_{i=1}^{N_I} \lambda_i \varphi_i \varphi_i^T \quad (21)$$

where $\lambda_1 \geq \dots \geq \lambda_i \geq \dots \geq \lambda_{N_I}$ are the respective eigenvalues of eigenvectors φ_i . SSP can be approximated with the first Q eigenvectors as

$$\mathbf{c} = \mathbf{c}_0 + \sum_{i=1}^Q a_i \varphi_i \quad (22)$$

where a_i and φ_i are called the i th EOF coefficient and EOF, respectively.

C. Objective Function

Parameter estimation is carried out by maximizing the normalized Bartlett power objective function of the form

$$B(\mathbf{a}, \mathbf{x}) = \frac{1}{N_F} \sum_{q=1}^{N_Q} \frac{|\mathbf{h}_q^H \mathbf{d}_q|}{\|\mathbf{d}_q\| \|\mathbf{h}_q\|} \quad (23)$$

where:

- $0 \leq B(\mathbf{a}, \mathbf{x}) \leq 1$, and a perfect match between measured acoustic field and modeled acoustic field is found when $B(\mathbf{a}, \mathbf{x}) = 1$;
- $\mathbf{a} = [a_1 \dots a_i \dots a_Q]$ is the EOF coefficient vector, and \mathbf{x} denotes other parameters to be estimated;
- $\mathbf{h}_q = [\tilde{p}(\mathbf{r}_0, z_1, \omega_q) \dots \tilde{p}(\mathbf{r}_0, z_M, \omega_q)]^T$ is the modeled acoustic field or replica field calculated using M1, M2, or M3 at receiver frequency ω_q . M is the number of elements of the VLA, and N_Q is the number of receiver frequencies to be used;
- \mathbf{d}_q is the measured acoustic field vector of the VLA at receiver frequency ω_q ;
- $(\cdot)^H$ denotes the conjugate transpose of a matrix, $|\cdot|$ denotes the modulus of a complex number, and $\|\cdot\|$ is the Euclidean norm of a vector.

When (13) is satisfied, i.e., the range aperture is large enough to resolve the adjacent Doppler shifted frequencies, the objective function can be derived as follows. According to (6) and (14), the received acoustic field can be approximated as

$$\begin{aligned} \tilde{p}(\mathbf{r}_0, z, \omega_q) &\simeq T\psi(\mathbf{r}_0, z, \omega_q) \\ &\simeq \frac{iT}{4\rho(z_s)} S(\omega_s) \Psi_{n_q}(z; \omega_q) \Psi_{n_q}(z_s; \omega_q) H_0^{(1)}(k_{rn_q}^q r_0) \\ &= \xi_q \Psi_{n_q}(z; \omega_q) \end{aligned} \quad (24)$$

where $\xi_q = iT/4\rho(z_s)S(\omega_s)\Psi_{n_q}(z_s; \omega_q)H_0^{(1)}(k_{rn_q}^q r_0)$, and the modal depth function $\Psi_{n_q}(z; \omega_q)$ is independent of source depth z_s and range r_0 . Thus one can write \mathbf{h}_q as

$$\mathbf{h}_q = \xi_q \Psi_{n_q}(\omega_q) \quad (25)$$

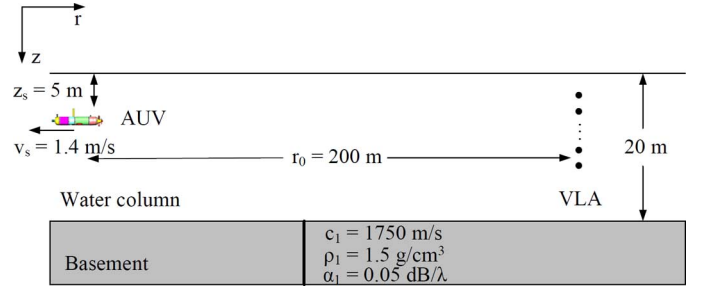


Fig. 6. Simulation scenario.

where $\Psi_{n_q}(\omega_q) = [\Psi_{n_q}(z_1; \omega_q) \dots \Psi_{n_q}(z_M; \omega_q) \dots \Psi_{n_q}(z_M; \omega_q)]^T$. Then the objective function can be derived as

$$\begin{aligned} B(\mathbf{a}, \mathbf{x}) &= \frac{1}{N_Q} \sum_{q=1}^{N_Q} \frac{|(\xi_q \Psi_{n_q}(\omega_q))^H \mathbf{d}_q|}{\|\mathbf{d}_q\| \|\xi_q \Psi_{n_q}(\omega_q)\|} \\ &= \frac{1}{N_Q} \sum_{q=1}^{N_Q} \frac{|(\Psi_{n_q}(\omega_q))^H \mathbf{d}_q|}{\|\mathbf{d}_q\| \|\Psi_{n_q}(\omega_q)\|}. \end{aligned} \quad (26)$$

We can see that the objective function is independent of source depth z_s and range r_0 . Hence, for SSP inversion, we do not need to consider the effect of source depth and range uncertainties; in addition, the number of parameters to be estimated can be reduced. Although the required condition is hard to meet, the discussion here will help analyse the simulation and experimental results.

IV. SIMULATIONS

In this section we address four issues relevant to the approach developed. Section IV-A evaluates the Doppler shifted frequencies and the minimum range aperture the AUV needs to traverse to resolve the adjacent Doppler shifted frequencies. Section IV-B investigates the field sensitivity of M1. Section IV-C compares M2 and M3 against M1. Finally in Section IV-D, unknown parameters are estimated with synthetic data.

Simulations are performed in a "realistic synthetic" scenario corresponding to the experimental setup. Consider a range-independent waveguide environment shown in Fig. 6, which consists of water column and basement. The values of the geoacoustic parameters of the basement are empirical ones. As mentioned before, the VLA consists of 16 elements with an equal spacing of 1 m and spans the water column from 1.5 to 16.5 m. The AUV is deployed to move radially away from the VLA at a constant depth of 5 m with a speed of 1.4 m/s. The frequency of radiation noise is 13 896 Hz. SSP is described by the first two EOFs with EOF1 coefficient $a_1 = -5.9$ and EOF2 coefficient $a_2 = -0.8$. A normal mode propagation model KRAKEN [20] is used to compute the wavenumbers and modal depth functions.

A. Doppler Shifted Frequencies

Based on the approximate solution for ω_r^l and $k_{rn_l}^l$ described in the Appendix, the Doppler shifted frequencies as a function of the mode number and the minimum range aperture [as defined by (13)] to resolve the adjacent Doppler shifted frequencies or modes are shown in Fig. 7. Leaky

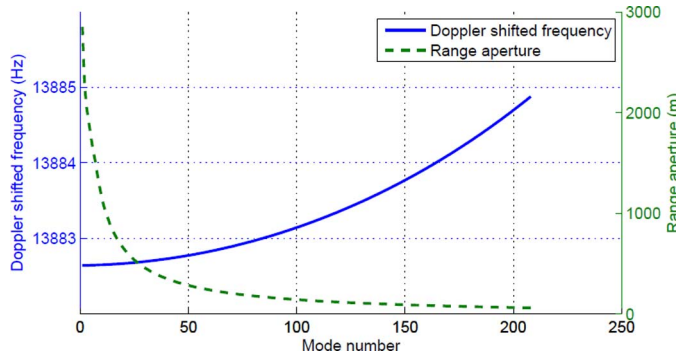


Fig. 7. Doppler shifted frequencies as a function of the mode number (left Y-axis); the minimum range aperture that the AUV needs to traverse to resolve the adjacent Doppler frequencies or modes (right Y-axis). The results are based on the given configuration shown in Fig. 6.

modes, i.e., the modes whose grazing angles are above the critical angle of 33.7° , are not plotted in Fig. 7. Because the AUV is moving radially away from the VLA, the Doppler shifted frequencies are lower than the frequency of the radiation noise 13 896 Hz. The minimum range apertures to resolve the first two Doppler shifted frequencies and the last two Doppler shifted frequencies are approximately 2800 m and 60 m, respectively. When the range aperture is not enough, according to (10), the frequency response of the received field is a weighted sum of the modal components, and the weights are mainly dependent on the frequency band $2/T$. Thus, the integration interval T will affect the received field, and then affect the performance of the inversion. Because lower Doppler shifted modal components (lower order modes or lower grazing angles) are less sensitive to the geoacoustic parameters, we can filter the received field accordingly to reduce the inversion uncertainty due to the uncertainty of those parameters.

B. Field Sensitivity of M1

We use M1 to generate noise free synthetic data for sensitivity analysis. For each parameter, a sensitivity plot is created by sweeping the parameter under test in the objective function while keeping the rest of the parameters at their individual true values. The received field at 13 883 Hz is used. When the integration interval equals 1 s, the receiver frequency of 13 883 Hz is used for inversion, which is mainly composed of the Doppler shifted modal components in a frequency band of 2 Hz centered at 13 883 Hz. These modal components correspond to modes 1 to 165, whose grazing angles are less than the critical angle. When the integration interval equals 5 s, the corresponding modes are 57 to 108.

Sensitivity plots for eleven parameters (EOF1 coefficient a_1 and EOF2 coefficient a_2 ; source range r_0 , depth d_s , velocity v_s , and frequency f_s ; water column depth D and depth of the 1st element of VLA z_1 ; bottom velocity c_1 , density ρ_1 , and attenuation α_1) with M1 at $T = 1$ s and $T = 5$ s, respectively, are shown in Fig. 8. It is seen that EOF1 coefficient a_1 is less sensitive than EOF2 coefficient a_2 , and a_2 becomes less sensitive when T increases to 5 s. As can be seen from Fig. 2(b), the second EOF represents the variability close to the surface. Hence it affects more the higher order modes (higher grazing

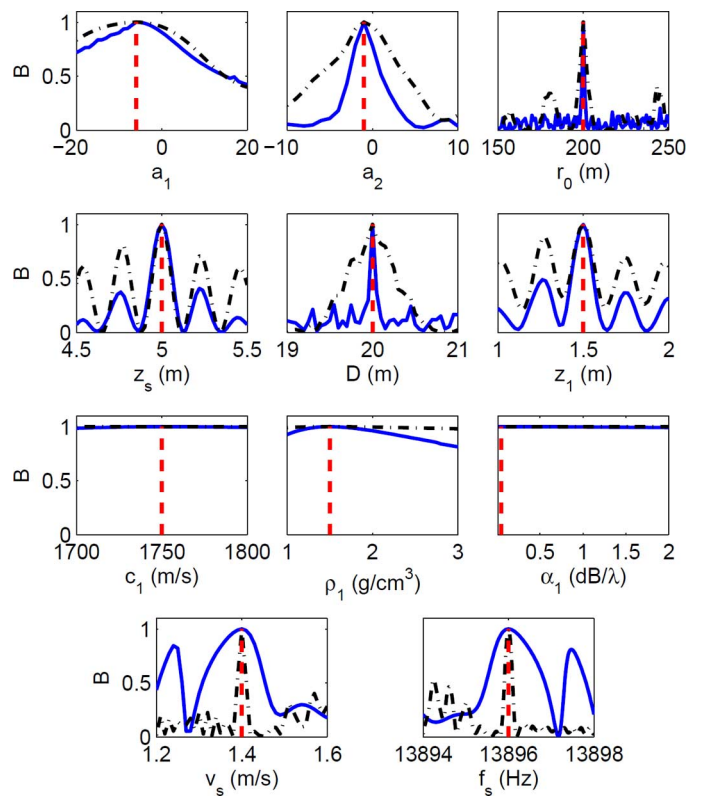


Fig. 8. Sensitivity plots for eleven parameters of the radial mission at different integration intervals: $T = 1$ s (solid line); $T = 5$ s (dash-dotted line). The dashed line indicates the true parameter value.

angles). When using a longer integration time T , as for receiver frequency 13 883 Hz, the weights of higher order modes decrease, which will reduce the sensitivity of a_2 . The range and depth of AUV are less sensitive when T increases, which agrees with (26), i.e., the objective function will be independent of the source range and depth when the range aperture is large enough. The water depth and the depth of the 1st element of VLA become less sensitive when T increases. The grazing angles of the modal components (whose Doppler frequencies are in the frequency band $2/T$) are from 0° to 20.7° (modes 1 to 165) when $T = 1$ s, and from 8.9° to 16.7° (modes 57 to 108) when $T = 5$ s. For a source depth of 5 m and water depth of 20 m, it takes 0 to 2 bottom bounces for the modal components to reach the VLA. From Fig. 8, the sensitivity plots for the bottom geoacoustic model parameters at $T = 1$ s are essentially flat, and this is also the case for $T = 5$ s. Hence the bottom properties are not significantly sensitive.

C. Comparison of M1, M2, and M3

To illustrate how the simplified models match with M1, first we evaluate the pressure values of M2, M3 with that of M1 at different integration intervals under the true parameters. As shown in Fig. 9, M2 has a large matched value, which approaches 1 as T increases. Noticed that, as T increases, the bandwidth decreases. The pressure value of M1 is mainly dependent on the Doppler shifted modal components which are in a bandwidth of $2/T$ centered at the receiver frequency, and $\psi(\mathbf{r}_0, z, \omega_r^l)$ is more approximate to $\psi(\mathbf{r}_0, z, \omega, k_{rl})$ when ω_r^l

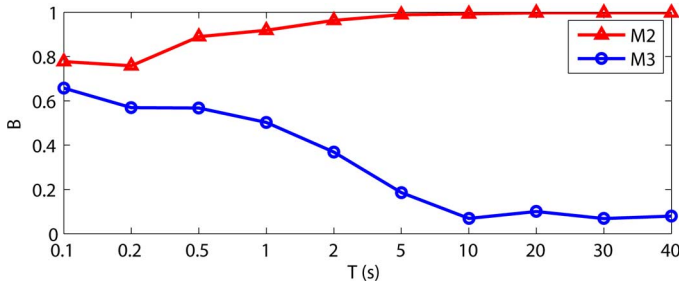


Fig. 9. Matching values of the simplified models at different integration intervals.

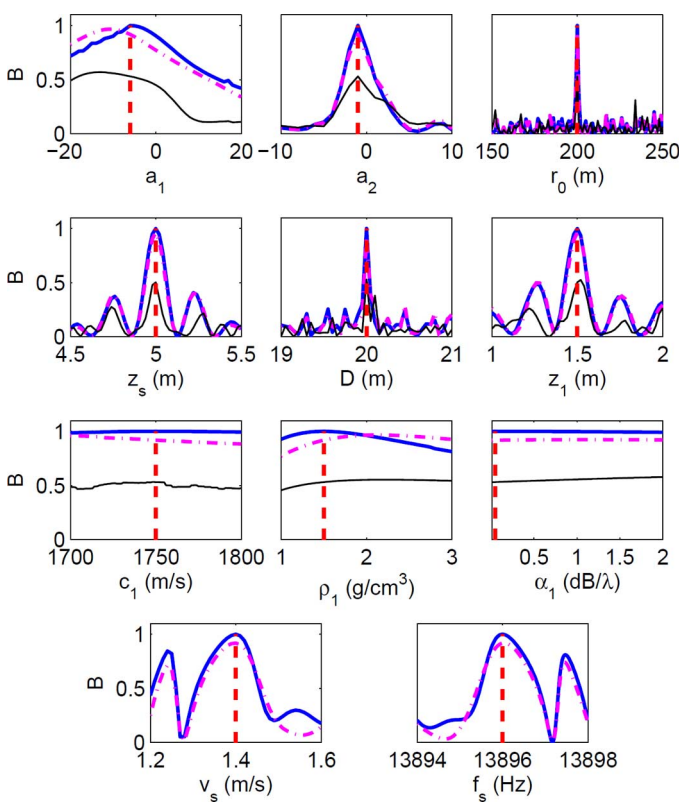


Fig. 10. Sensitivity plots of different simplified models at $T = 1$ s: M1 (thick solid line); M2 (dash-dotted line); M3 (thin solid line). The dashed line indicates the true parameter value.

is closer to ω . The matched value of M3 are smaller compared with M2, and it approaches the value of M2 as T decreases. This is because, as T decreases, the weight of each modal component approaches the same value, which makes M3 approaching M2.

Now we present correlations between M1 and different simplified models. Fig. 10 is the sensitivity plots of M2 and M3 at $T = 1$ s. The solid line repeats the regular sensitivity plot in Fig. 8. We can find that the sensitivity plot of M2 is very similar to that of M1. Although the correlation of M3 is not so high as that of M2, the shape of the sensitivity plot is somewhat similar to that of M1. Fig. 11 is the sensitivity plots of M2 and M3 at $T = 5$ s. We can find that the sensitivity plot of M2 is more similar to that of M1 compared with the result in Fig. 10, while M3 is mismatched.

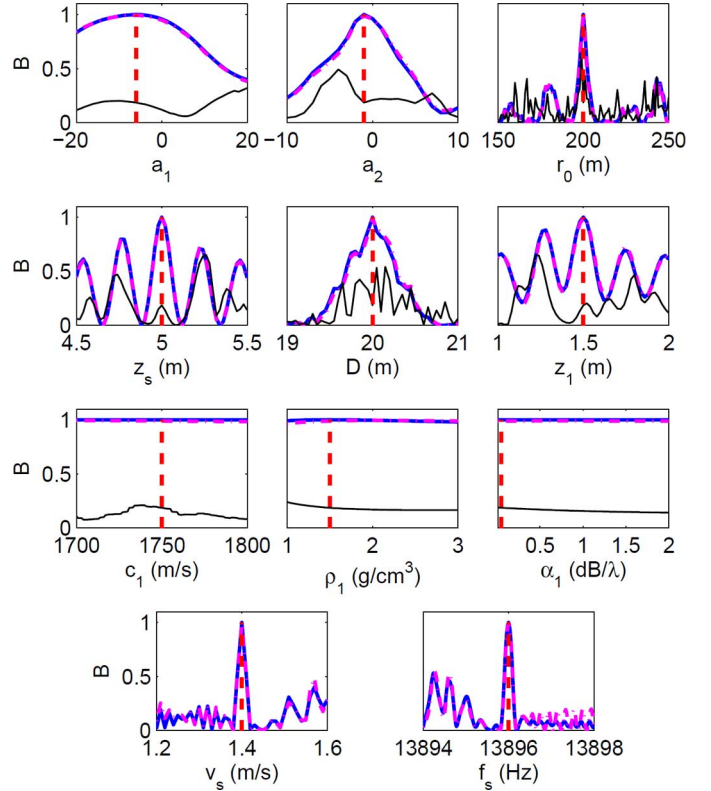


Fig. 11. Sensitivity plots of different simplified models at $T = 5$ s: M1 (thick solid line); M2 (dash-dotted line); M3 (thin solid line). The dashed line indicates the true parameter value.

D. Comparison of M2 and M3 for Synthetic Data Inversion

We use M2 and M3 for synthetic data inversion. The synthetic data are computed using M1, with spatially white, complex Gaussian noise added to the Doppler shifted modal components to yield an average SNR of 20 dB, i.e.,

$$\text{SNR} = 10 \log_{10} \frac{\sum_{l=1}^L \sum_{m=1}^M |\psi(\mathbf{r}_0, z_m, \omega_r^l)|^2}{LM\sigma^2} = 20 \text{ dB} \quad (27)$$

where σ^2 denotes the variance of the noise. Genetic algorithms (GA) [21], [22] are applied for the estimates of the EOF coefficients and other parameters. The values of the GA parameters are as follows: population size, 120; selection, 0.5; crossover, 0.8; mutation, 0.1; iterations, 150.

To reduce the number of parameters to be estimated, we can fix the values of the parameters which are insensitive (e.g., the bottom parameters). In addition, parameter coupling causes difficulty in determining the best matched model, as different parameter combinations will produce very similar (large) matched values. From Fig. 8, we can find that the sensitivity plots for the source depth d_s and the depth of the 1st element of the VLA z_1 are similar. This is because they act in a consistent way through the modal depth function. Fig. 12(a) further illustrates that they are coupled since the mainlobe and the sidelobes with large matched values are elongated along the diagonal direction. Besides those two parameters, since the velocity of the AUV v_s and the source frequency f_s both affect the receiver frequency through (5), we can see a coupling between them

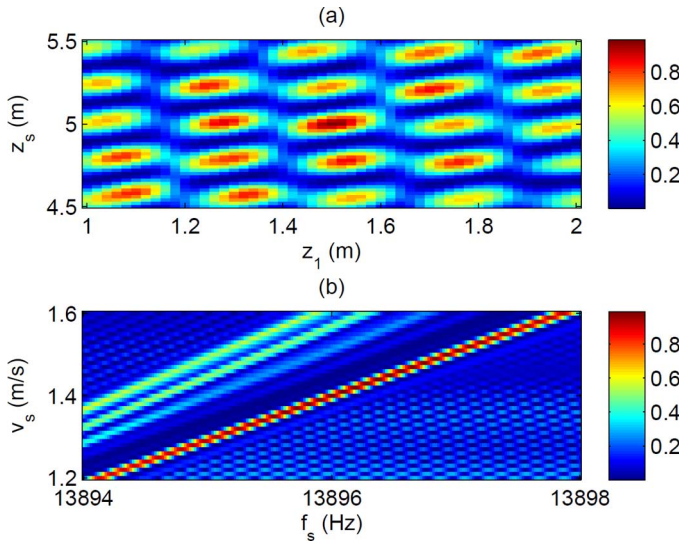


Fig. 12. Sensitivity plots for: (a) the depth of the 1st element of the VLA z_1 and the source depth z_s ; (b) the source frequency f_s and velocity v_s .

TABLE I
INVERSION PARAMETERS AND SEARCH BOUNDS

Model parameters	Lower bound	Upper bound
EOF1 coef., a_1	-20	20
EOF2 coef., a_2	-10	10
Src range, r_0 (m)	150	250
Src depth, z_s (m)	4.5	5.5
Water depth, D (m)	19	21
Src vel., v_s (m/s)	1.2	1.6
Rcv depth, z_1 (m)	1.4	1.6
Src freq., f_s (Hz)	13 895.5	13 896.5

from Fig. 12(b). To search the coupled parameters in a more efficient way, we adopt the approach in [23], i.e., narrowing the search bounds for z_1 and f_s according to their measurement/estimate accuracy. The inversion parameters and the associated searching bounds are tabulated in Table I. Since M3 is independent of the source velocity, it can not be used to estimate v_s and f_s . In the table, src denotes the source..

Figs. 13 and 14 are scatter plots illustrating the parameters sampled during GA inversions using M2 and M3, respectively. Fig. 13(a) is the result using M2 at $T = 1$ s with single frequency 13 883 Hz. The maximum matched value is 0.86. The estimated EOF1 coefficient a_1 has a negative bias, and the distribution is flat, which is consistent with the sensitivity plot in Fig. 10. Both EOF2 coefficient a_2 and source range r_0 have relative good estimate results, since the objective function is sensitive to those parameters, as shown in Fig. 10. Since source depth z_s is coupled with z_1 and velocity v_s is coupled with f_s , they are not well estimated. Water depth D is not well estimated either. This is most likely for that the source range and water depth are

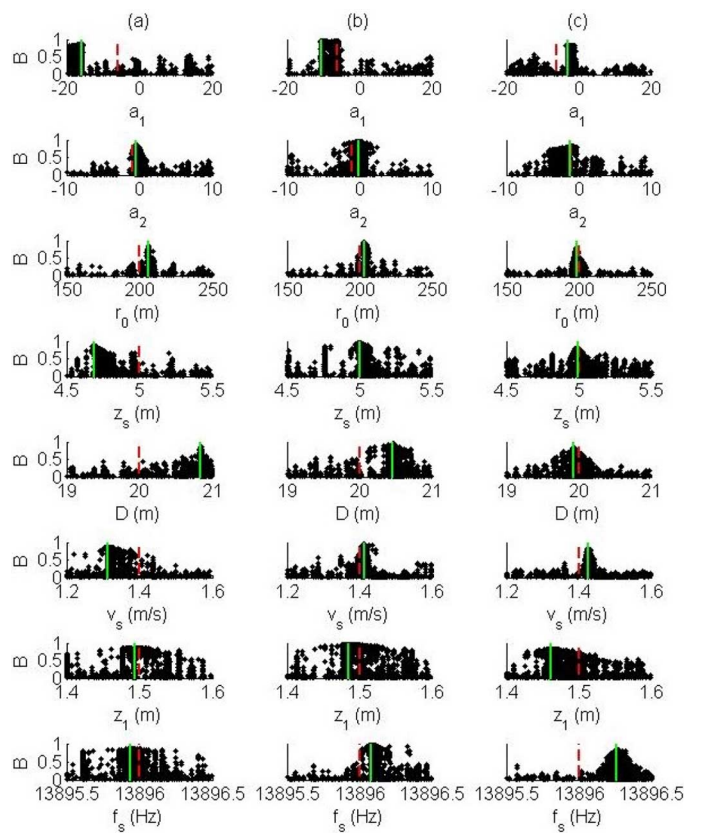


Fig. 13. Scatter plots of GA search using M2. (a) At $T = 1$ s with single frequency of 13 883 Hz. (b) At $T = 5$ s with single frequency of 13 883 Hz. (c) At $T = 5$ s with frequencies of 13 882.8, 13 883, 13 883.2, and 13 883.4 Hz. The dashed line indicates the true value, and the solid line indicates the final inversion result.

coupled, especially when $T = 5$ s. As shown in Fig. 15, source range and water depth are biased indeed in the same direction, which is consistent with the inversion results. When $T = 5$ s, as shown in Fig. 13(b), the maximum matched value increases to 0.95. The distribution of the EOF2 coefficient is not so sharp as that of $T = 1$ s, and the distributions of v_s and f_s are sharper compared with that of $T = 1$ s, which are all consistent with the sensitivity analysis shown in Fig. 8. Fig. 13(b) only utilizes a single frequency 13 883 Hz; as can be seen from (17), when $T = 5$ s the number of modes that contribute to the acoustic field is less than that of $T = 1$ s. To include more modes, we use receiver frequencies of 13 882.8, 13 883, 13 883.2, and 13 883.4 Hz for inversion. As shown in Fig. 13(c), although the maximum matched value reduces to 0.82, the distributions of parameters become more compact.

The inversion performance with M3 is as good as that of M2 when $T = 1$ s. However, as shown in Fig. 14(b), the performance degrades when T increases to 5 s. Utilizing multiple receiver frequencies, as shown in Fig. 14(c), does not improve the final estimates.

V. EXPERIMENTAL DATA ANALYSIS

Based on the simulations, we process experimental data of the radial mission. We compare the inversion performance of M2 and M3 at $T = 1$ s and $T = 5$ s. The frequency resolution of 1-s data is 1 Hz, and 0.2 Hz for 5-s data. The first two EOF

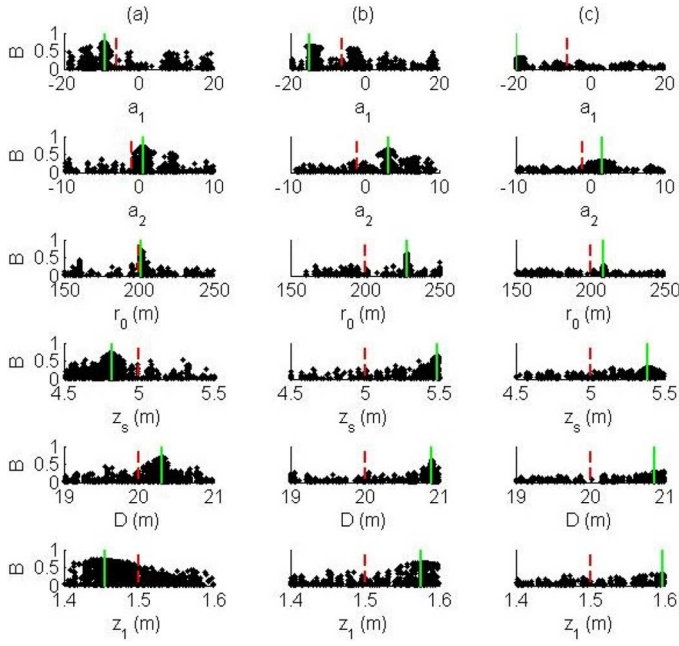


Fig. 14. Scatter plots of GA search using M3. (a) At $T = 1$ s with single frequency of 13 883 Hz. (b) At $T = 5$ s with single frequency of 13 883 Hz. (c) At $T = 5$ s with frequencies of 13 882.8, 13 883, 13 883.2, and 13 883.4 Hz. The dashed line indicates the true value, and the solid line indicates the final inversion result.

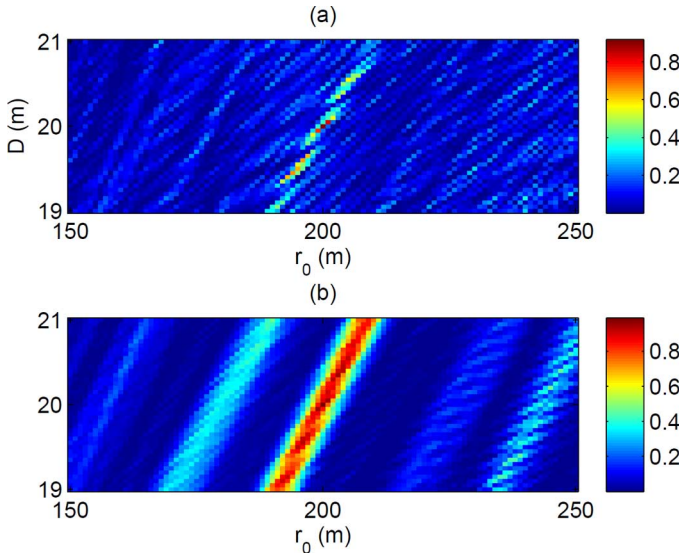


Fig. 15. Sensitivity plots for water depth D and source range r_0 . (a) $T = 1$ s. (b) $T = 5$ s.

coefficients are used to describe the SSP. The errors in the SSP estimation can be evaluated by the depth-integrated root mean square error (RMSE) [24] metric, which essentially calculates the difference between the true sound speed (the sound speed measured with CTD, denoted by c_{true}) and the estimated sound speed (c_{est}), and then sums across depth to provide a single quantity defined by

$$\Delta c_{\text{RMS}} = \sqrt{\frac{1}{N_Z} \sum_{z=1}^{N_Z} [c_{\text{true}}(z) - c_{\text{est}}(z)]^2}. \quad (28)$$

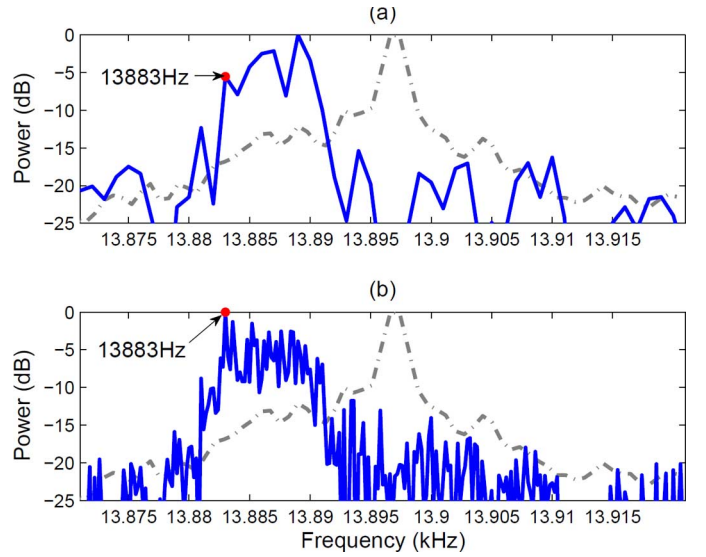


Fig. 16. Power spectral density of the data around the point $(-150 \text{ m}, -150 \text{ m})$ of Mission 2. (a) $T = 1$ s. (b) $T = 5$ s. Dash-dotted line repeats the power spectral density of Mission 1 for source frequency of 13 896 Hz in Fig. 4.

The data around the point $(-150 \text{ m}, -150 \text{ m})$ of Mission 2 in Fig. 1 are used for processing, and Fig. 16 shows the received power spectral density for source frequency of 13 896 Hz when $T = 1$ s and $T = 5$ s. The power spectral density of Mission 1 for source frequency of 13 896 Hz is overlaid so that the Doppler effect can be clearly seen. We can observe that the Doppler shifted frequencies are from 13 881 to 13 891 Hz. According to the environment and source velocity given in the paper, we can calculate there are 326 modes. The grazing angle of Doppler shifted frequency 13 891 Hz is about 68° , which is above the critical angle of 33.7° . Thus a large number of the modes are leaky modes.

Although the AUV was deployed to run at 5-m depth, the depth measured with pressure sensor was 4.85 m. The 14th CTD cast which was taken just before Mission 2 started is treated as the reference SSP. The first two EOF coefficients are $a_1 = -5.9$ and $a_2 = -0.8$, respectively. The depth-integrated RMSE of the synthesized SSP with the two EOF coefficients is 0.06 m/s. The inversion parameters and searching bounds are the same as in the simulations (see Table I).

Figs. 17 and 18 are scatter plots illustrating the parameters sampled during GA inversions using M2 and M3, respectively. Fig. 17(a) is the result using M2 at $T = 1$ s with single frequency 13 883 Hz. The maximum matched value is 0.58. The estimate of EOF1 coefficient a_1 has a negative bias, which is consistent with the simulation result. EOF2 coefficient a_2 and source range r_0 have relatively good estimated results, for the objective function is sensitive to those parameters, as shown in Fig. 10. When $T = 5$ s, the maximum matched value is 0.65 [see Fig. 17(b)]. The distribution of EOF2 coefficient is not so sharp as that of $T = 1$ s, and the distributions of source speed and frequency become sharper compared to those of $T = 1$ s, which as well are consistent with the simulation results. To include more modes, we utilize receiver frequencies of 13 882.8, 13 883, 13 883.2, and 13 883.4 Hz for inversion. As shown in Fig. 17(c),

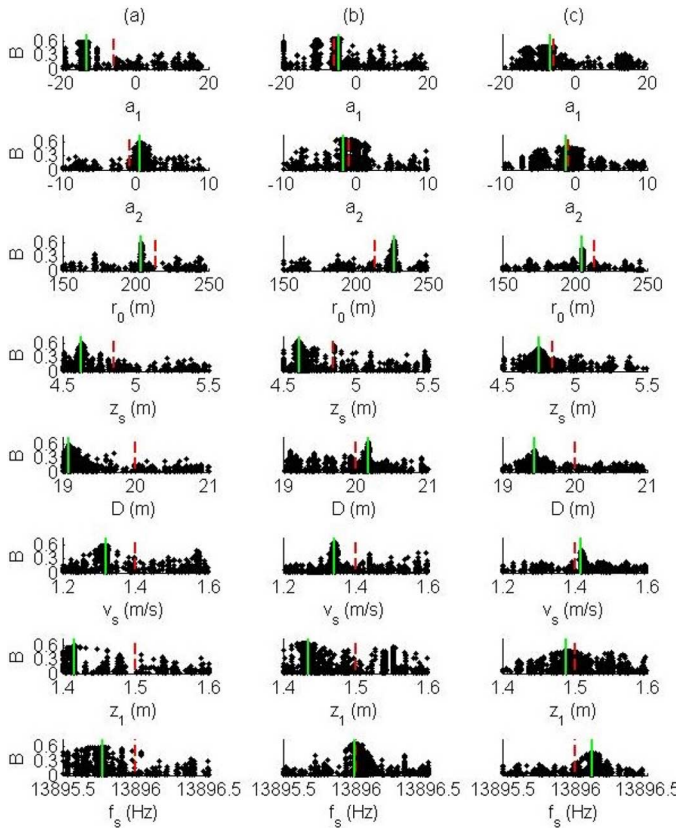


Fig. 17. Scatter plots of GA search using M2. (a) At $T = 1$ s with single frequency of 13 883 Hz. (b) At $T = 5$ s with single frequency of 13 883 Hz. (c) At $T = 5$ s with frequencies of 13 882.8, 13 883, 13 883.2, and 13 883.4 Hz. The dashed line indicates the reference value, and the solid line indicates the final inversion result.

although the maximum matched value reduces to 0.47, the distributions of parameters become more compact. The depth-integrated RMSE of SSP estimates of Figs. 17(a)–17(c) are 1.11, 0.27, and 0.14 m/s, respectively. Fig. 19 shows the three estimated water column SSPs along with the 14th CTD cast. We can see that the estimated SSP is biased along the entire water column when $T = 1$ s due to the relatively large estimated error of a_1 .

The estimated source depth has a negative bias, probably because the source depth is coupled with the depth of the 1st element of VLA z_1 [see Fig. 12(a)], and there is a measurement error of z_1 using the depth sensor. There is also a negative bias for the source velocity in Figs. 17(a) and 17(b). One reason can be that source velocity is coupled with the source frequency [see Fig. 12(b)], and there is an estimated error of the source frequency. The other possible reason is that the angle θ_s between the velocity vector and the radial vector connecting AUV and VLA is not exactly 180° , and then the estimates of source velocity is less than 1.4 m/s. Note that the maximum matched values are all less than 0.7. This is likely attributed to the fact that the radiation noise of the AUV is not a clean tone [see Fig. 3(a)], while M2 is based on the monochromatic source assumption. The other possible reason may be that the model used in the paper is derived based on range-independent environment, while the actual environment is range dependent, e.g., the water depth varying at different ranges.

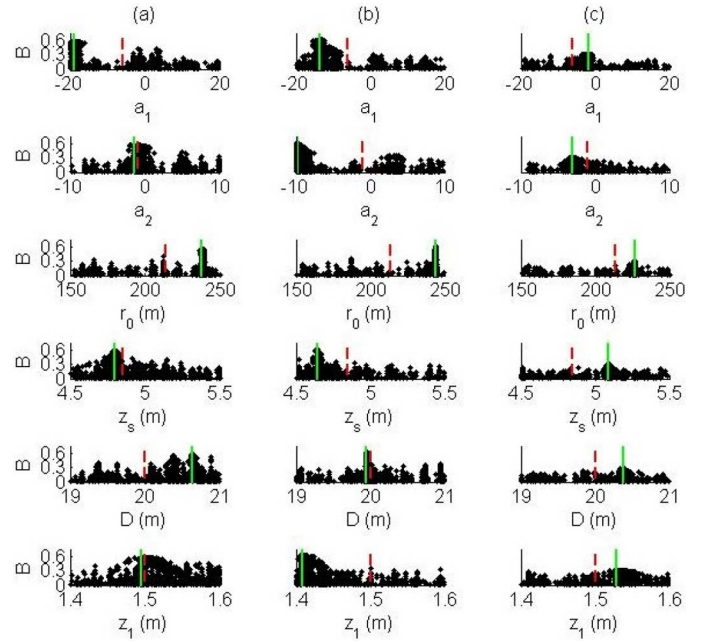


Fig. 18. Scatter plots of GA search using M3. (a) At $T = 1$ s with single frequency of 13 883 Hz. (b) At $T = 5$ s with single frequency of 13 883 Hz. (c) At $T = 5$ s with frequencies of 13 882.8, 13 883, 13 883.2, and 13 883.4 Hz. The dashed line indicates the reference value, and the solid line indicates the final inversion result.

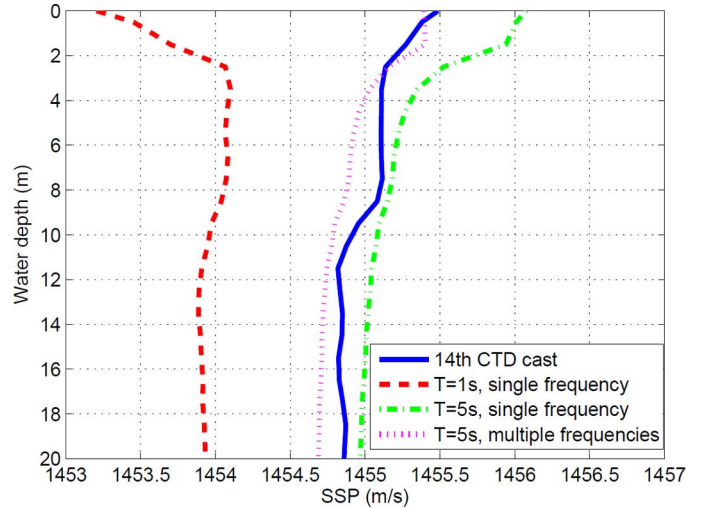


Fig. 19. SSP inversion results using experimental data with M2.

The inversion results that utilize M3 have reasonable estimates when $T = 1$ s. However, as shown in Fig. 18(b), the performance degrades when T increases to 5 s. Although utilizing multiple receiver frequencies has improved the final estimates (the depth-integrated RMSE of SSP is 0.77 m/s), the matched value is small and the distribution is flat [see Fig. 18(c)].

VI. CONCLUSION

In this paper we use the radiation noise of an AUV as the sound source to invert the range-independent SSP, together with the position and velocity of the AUV, and the water column depth. To incorporate source motion effects, the forward model

based on the waveguide Doppler and normal mode theory is applied to compute the replica field. Given the source frequency and water depth of this experiment, it is difficult to resolve the adjacent Doppler shifted frequencies. In that case, the frequency response of the received field is a weighted sum of modal components. An analytical solution of the forward model is obtained for arbitrary signal integration intervals with a monochromatic source, moving radially relative to the receiver. A simplified model is proposed to reduce the computational complexity, and the model matches well with the original model especially when the integration interval is large. The waveguide Doppler model is shown to be more effective compared with the model that does not consider the Doppler effect through simulation and experimental results. The distributions of parameters become more compact using multiple receiver frequencies at the cost of reduced matched value and increased computational effort. The parameters of high field sensitivity are well estimated except those mutually-coupled.

Note that the theory presented in this paper is based on the monochromatic source assumption, while the radiation noise of the AUV may not be a clean tone. This mismatch can affect the inversion performance. For deeper investigation of moving acoustic tomography, a source transducer mounted on the AUV to transmit arbitrary waveforms is desired. In addition, the waveguide Doppler model can be used as a forward acoustic model in state-space solution for SSP and source tracking with sequential Bayesian filtering.

APPENDIX

To obtain the approximate solution for ω_r^l and $k_{rn_l}^l$, we make the assumption that the wavenumbers of the adjacent Doppler shifted frequencies ω_r^l and ω_r^{l+1} are approximately equal, i.e., $k_{rm}^l \simeq k_{rm}^{l+1}$, $m = 1, 2, \dots$. The assumption is reasonable since the adjacent Doppler shifted frequencies are very close to each other [16]. Under this assumption we can use $k_{r(n_l+1)}^l$ to estimate ω_r^{l+1} with (5). The procedures to compute ω_r^l and $k_{rn_l}^l$ are as follows:

- 1) Compute the initial frequency (the Doppler shifted frequency whose grazing angle is zero) and the associated wavenumber. The initial angular frequency can be calculated using the Doppler shift formula [25] in free space as

$$\omega_r^1 = \frac{\omega_s c(z_s)}{(c(z_s) - v_s)} \quad (29)$$

where $c(z_s)$ is the sound speed at the source depth. Substituting (29) into (5) yields an estimate of the horizontal wavenumber $\hat{k}_{rn_1}^1$. Compute the horizontal wavenumbers k_{rm}^1 as per the static case evaluated at ω_r^1 , and order them so as $k_{r1}^1 > k_{r2}^1 > \dots$. Search the one that is closest to $\hat{k}_{rn_1}^1$, and assign the index value to n_1 . Then $k_{rn_1}^1$ is the horizontal wavenumber corresponding to angular frequency ω_r^1 .

- 2) Denote $k_{r(n_1+l)}^l$, $l = 1, 2, \dots$ as $\hat{k}_{r(n_1+l)}^{l+1}$. Substituting $\hat{k}_{r(n_1+l)}^{l+1}$ into (5) yields the $(l+1)$ th Doppler shifted frequency ω_r^{l+1} . Compute the horizontal wavenumbers as per the static case evaluated at ω_r^{l+1} , and then $k_{r(n_1+l)}^{l+1}$ is the wavenumber corresponding to angular frequency

ω_r^{l+1} . This step is repeatedly executed until $n_1 + l$ equals to the number of wavenumbers evaluated at frequency ω_r^{l+1} .

ACKNOWLEDGMENT

The authors would like to thank the AUV team members in Zhejiang University for their contribution and assistance during the experiment. They would also like to thank the anonymous reviews for valuable comments.

REFERENCES

- [1] W. Munk and C. Wunsch, "Ocean acoustic tomography: A scheme for large scale monitoring," *Deep-Sea Res. A*, vol. 26, pp. 123–161, 1979.
- [2] J. L. Spiesberger, P. J. Bushong, K. Metzger Jr., and T. G. Birdsall, "Ocean acoustic tomography: Estimating the acoustic travel time with phase," *IEEE J. Ocean. Eng.*, vol. 14, no. 1, pp. 108–119, Jan. 1989.
- [3] A. Tolstoy, O. Diachok, and L. N. Frazer, "Acoustic tomography via matched field processing," *J. Acoust. Soc. Amer.*, vol. 89, no. 3, pp. 1119–1127, Mar. 1991.
- [4] A. B. Baggeroer, W. A. Kuperman, and P. N. Mikhalevsky, "An overview of matched field methods in ocean acoustics," *IEEE J. Ocean. Eng.*, vol. 18, no. 4, pp. 401–424, Oct. 1993.
- [5] H. Schmidt, "AREA: Adaptive rapid environmental assessment," in *Impact of Littoral Environmental Variability of Acoust. Predictions and Sonar Performance*, N. G. Pace and F. B. Jensen, Eds. Norwell, MA, USA: Kluwer Academic Publishers, 2002, pp. 587–594.
- [6] H. Schmidt, J. G. Bellingham, and P. Elisseeff, E. Pouliquen, A. D. Kirwan, and R. T. Pearson, Eds., "Acoustically focused oceanographic sampling in coastal environments," in *Proc. Rapid Environ. Assessment Conf. Proc. Series CP-44 SACLANTCEN*, La Spezia, Italy, 1997, pp. 145–151.
- [7] P. Elisseeff, H. Schmidt, M. Johnson, D. Herold, N. R. Chapman, and M. M. McDonald, "Acoustic tomography of a coastal front in Haro Strait, British Columbia," *J. Acoust. Soc. Amer.*, vol. 106, no. 1, pp. 169–184, Jul. 1999.
- [8] J. D. Holmes, W. M. Carey, and J. F. Lynch, "Results from an autonomous underwater vehicle towed hydrophone array experiment in nantucket sound," *J. Acoust. Soc. Amer.*, vol. 120, no. 2, pp. EL15–EL21, Aug. 2006.
- [9] A. V. van Leijen, L. J. M. Rothkrantz, and F. C. A. Groen, "Acoustic inversion with self noise of an autonomous underwater vehicle to measure sound speed in marine sediments," in *Proc. 12th Int. Conf. Inf. Fusion*, Seattle, WA, USA, Jul. 2009, pp. 41–47.
- [10] N. P. Chotiros and V. Pallayil, "Seabed characterization using acoustic communication signals on an autonomous underwater vehicle with a thin-line towed array," *IEEE J. Ocean. Eng.*, vol. 38, no. 3, pp. 410–418, Jul. 2013.
- [11] C. F. Huang, P. Gerstoft, and W. S. Hodgkiss, "Effect of ocean sound speed uncertainty on matched-field geoacoustic inversion," *J. Acoust. Soc. Amer.*, vol. 123, no. 6, pp. EL162–EL168, Aug. 2008.
- [12] H. Schmidt and W. A. Kuperman, "Spectral and modal representations of the Doppler-shifted field in ocean waveguides," *J. Acoust. Soc. Amer.*, vol. 96, no. 1, pp. 386–395, Jul. 1994.
- [13] K. E. Hawker, "A normal mode theory of acoustic Doppler effects in the oceanic waveguide," *J. Acoust. Soc. Amer.*, vol. 65, no. 3, pp. 675–681, Mar. 1979.
- [14] F. B. Jensen, W. A. Kuperman, M. B. Porter, and H. Schmidt, *Computational Ocean Acoustic: Modern Acoustics and Signal Processing*, 2nd ed. New York, NY, USA: Springer-Verlag, 2011, pp. 623–629.
- [15] B. A. Tan, P. Gerstoft, C. Yardim, and W. S. Hodgkiss, "Broadband synthetic aperture geoacoustic inversion," *J. Acoust. Soc. Amer.*, vol. 134, no. 1, pp. 312–322, Jul. 2013.
- [16] S. C. Walker, P. Roux, and W. A. Kuperman, "Modal Doppler theory of an arbitrarily accelerating continuous-wave source applied to mode extraction in the oceanic waveguide," *J. Acoust. Soc. Amer.*, vol. 122, no. 3, pp. 1426–1439, Sep. 2007.
- [17] M. Zhang, Y. X. Xu, B. Li, D. N. Wang, and W. Xu, "A modular autonomous underwater vehicle for environmental sampling: System design and preliminary experimental results," in *Proc. MTS/IEEE OCEANS Conf.*, Taipei, Taiwan, Apr. 2014.
- [18] L. R. LeBlanc and F. H. Middleton, "An underwater acoustic sound velocity data model," *J. Acoust. Soc. Amer.*, vol. 67, no. 6, pp. 2055–2062, Jun. 1980.

- [19] J. D. Holmes, W. M. Carey, and J. F. Lynch, "An overview of unmanned underwater vehicle noise in the low to mid frequencies bands," in *Proc. Meet. Acoust.*, 2010, vol. 9, p. 065007.
- [20] M. B. Porter, "The KRAKEN normal mode program," in *SACLANT Undersea Res. Centre*, La Spezia, Italy, 1991.
- [21] P. Gerstoft, "Inversion of seismoacoustic data using genetic algorithms and a posteriori probability distributions," *J. Acoust. Soc. Amer.*, vol. 95, no. 2, pp. 770–782, Feb. 1994.
- [22] M. Musil, M. J. Wilmut, and N. R. Chapman, "A hybrid simplex genetic algorithm for estimating geoacoustic parameters using matched-field inversion," *IEEE J. Ocean. Eng.*, vol. 24, no. 3, pp. 358–369, Jul. 1999.
- [23] M. R. Fallat, P. L. Nielsen, and S. E. Dosso, "Hybrid geoacoustic inversion of broadband mediterranean sea data," *J. Acoust. Soc. Amer.*, vol. 107, no. 4, pp. 1967–1977, Apr. 2000.
- [24] O. Carrière, J. P. Hermand, and J. V. Candy, "Inversion for time-evolving sound-speed field in a shallow ocean by ensemble kalman filtering," *IEEE J. Ocean. Eng.*, vol. 34, no. 4, pp. 586–602, Oct. 2009.
- [25] L. E. Kinsler, A. R. Frey, A. B. Coppens, and J. V. Sanders, *Fundamentals of Acoustics*, 4th ed. New York, NY, USA: Wiley, 2000, pp. 453–454.



Ming Zhang received the B.E. degree in electrical engineering from Zhejiang University, Hangzhou, China, in 2009, where he is currently working toward the Ph.D. degree in the Department of Information Science and Electronic Engineering.

His research interests include ocean acoustic inverse problems and the development and use of autonomous underwater vehicles.



Wen Xu (S'97–A'01–M'02–SM'04) received the B.E. degree in electrical engineering from the University of Science and Technology of China, Hefei, China, in 1990, the M.S. degree in acoustics from the Institute of Acoustics, Chinese Academy of Sciences, Beijing, China, in 1993, and the Ph.D. degree in oceanographic engineering from the Massachusetts Institute of Technology (MIT), Cambridge, MA, USA, in 2001.

From 1993 to 1996, he was a Research Engineer with the Institute of Acoustics, Chinese Academy of Sciences. He was with the Ocean Acoustics Group, MIT, as a Research Scientist from 2001 to 2002, and with the Teledyne RD Instruments, San Diego, CA, USA, as a Research Scientist/Senior Research Scientist from 2003 to 2007. Currently, he is a Professor and the Associate Chair at the Department of Information Science and Electronic Engineering, Zhejiang University, Hangzhou, China. His research has concerned statistical and array signal processing in general and in applications to sonar, radar, and communication systems, and most recently to underwater sensor network.



Yuan-xin Xu received the B.S., M.S., and Ph.D. degrees in electrical engineering from Zhejiang University, Hangzhou, China, in 1995, 1998, and 2003, respectively.

He is an Associate Professor at the Department of Information Science and Electronic Engineering, Zhejiang University. His current research interests include underwater robot, signal processing, communications and networking.